

Supporting Information for

Oblique convergence causes both thrust and strike-slip ruptures during the 2021 M 7.2 Haiti earthquake

Ryo Okuwaki^{1,2,3}& Wenyuan Fan⁴

¹Mountain Science Center, University of Tsukuba, Tsukuba, Ibaraki 305-8572, Japan

²Faculty of Life and Environmental Sciences, University of Tsukuba, Tsukuba, Ibaraki 305-8572, Japan

³COMET, School of Earth and Environment, University of Leeds, Leeds LS2 9JT, UK

⁴Scripps Institution of Oceanography, UC San Diego, La Jolla, California 92093, USA

Contents

- Text S1
- Figures S1–S10

Corresponding author: Ryo Okuwaki, rokuwaki@geol.tsukuba.ac.jp

Text S1. Faulting interaction and triggering of large earthquakes in Haiti

To investigate the triggering mechanism, we calculate the static Coulomb failure stress changes (King et al., 1994; Lin & Stein, 2004; Toda et al., 2005; Wang et al., 2021) on faults with the E2 geometry from the E1 rupture (Fig. S6). We find minor Coulomb stress changes (<20 kPa at 10 km) near the E2 domain (Fig. S6). The stress changes are positive and may have brought the fault closer to failure. However, such an impact would be marginal given the small perturbation values (<20 kPa), suggesting that the static stress change from E1 was unlikely the sole nucleation cause of E2. We also test the Coulomb stress effects of E1 on the western strand of EPGF. We find greater static stress changes in this case comparing to the E2 case when assuming a target fault with a left-lateral strike-slip geometry along EPGF (Fig. S6). This further confirms the importance of the dynamic effects as an EPGF strand should have slipped if the static stress change was the key driving factor.

The 2021 Haiti earthquake locates ~96 km apart from the 2010 Haiti earthquake, and both earthquakes involve blind thrust faults in a similar fashion (Hayes et al., 2010). In order to evaluate a possible interaction between the 2010 and 2021 Haiti earthquakes, we calculate the Coulomb stress changes on the E1 fault induced by the 2010 Haiti earthquake (Hayes et al., 2010) (Fig. S7). The result shows positive Coulomb stress perturbations near the 2021 hypocenter, but the stress changes are negligible at a 12 km depth as <10 kPa. Our model of simple Coulomb stress interactions does not predict an obvious causal relationship between the two earthquakes (Fig. S7). Intriguingly, the 2010 Haiti earthquake would cause a greater static stress perturbation at the 2021 hypocenter if the receiver fault shares the EPGF geometry (Fig. S7). We speculate that the static stress changes alone from the 2010 Haiti earthquake are unlikely to enable the failure (E1) of the 2021 Haiti earthquake.

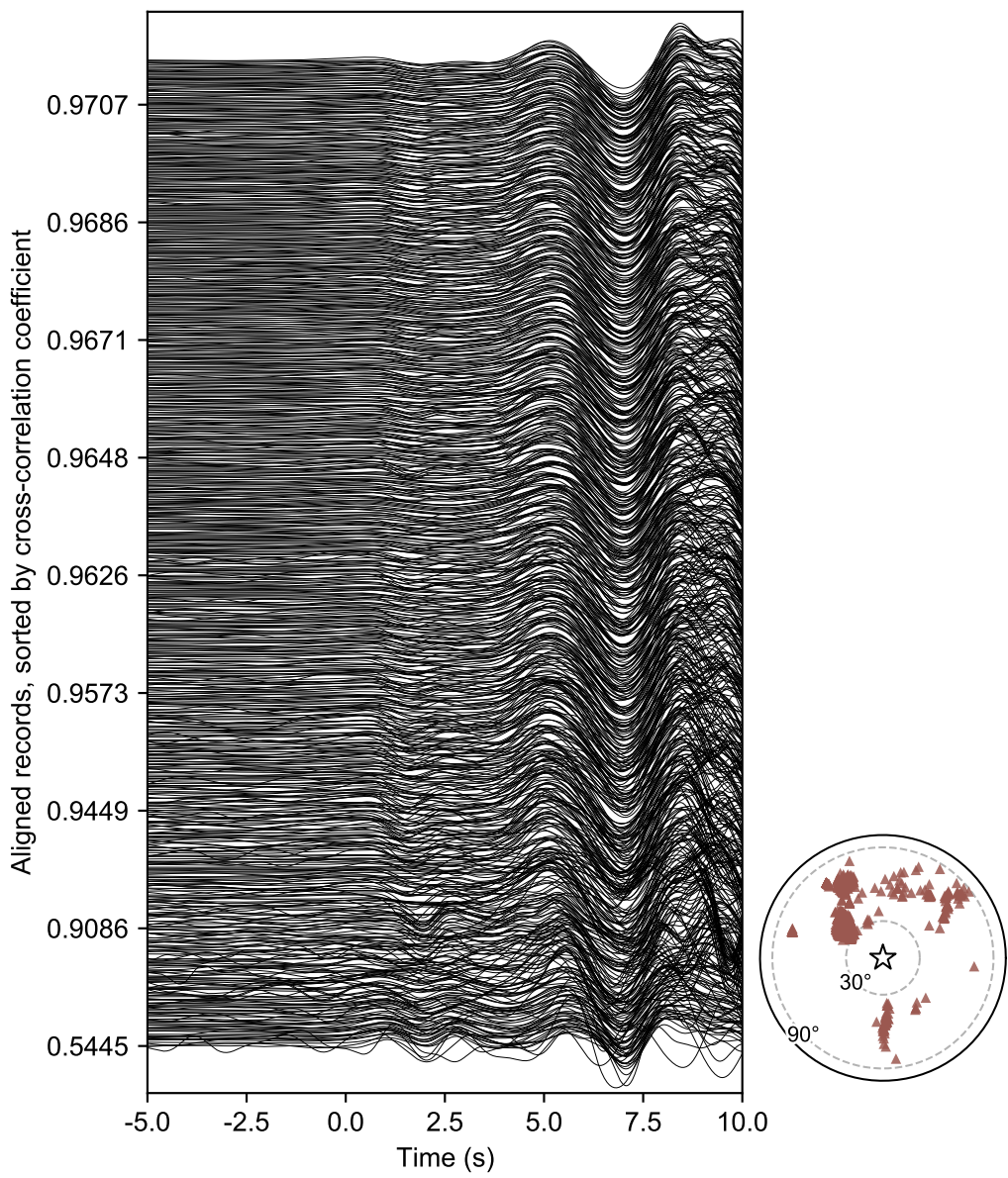


Figure S1. Self-normalized traces used for the back-projection analysis. The records are band-pass filtered at 0.2–1 Hz. The right panel shows the station distribution.

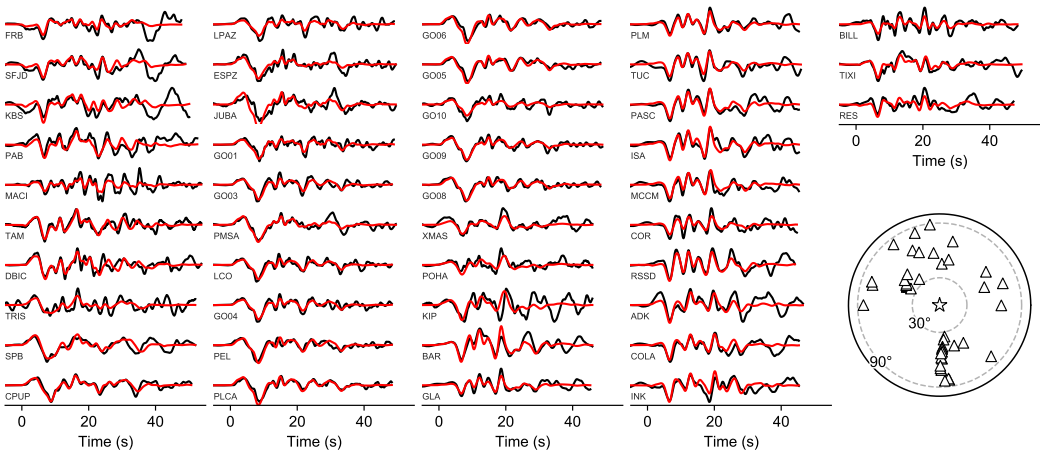


Figure S2. The observed (black) and synthetic (red) waveforms of the optimal finite-fault model. The station code is shown in each panel. The lower-right panel shows the station distribution.

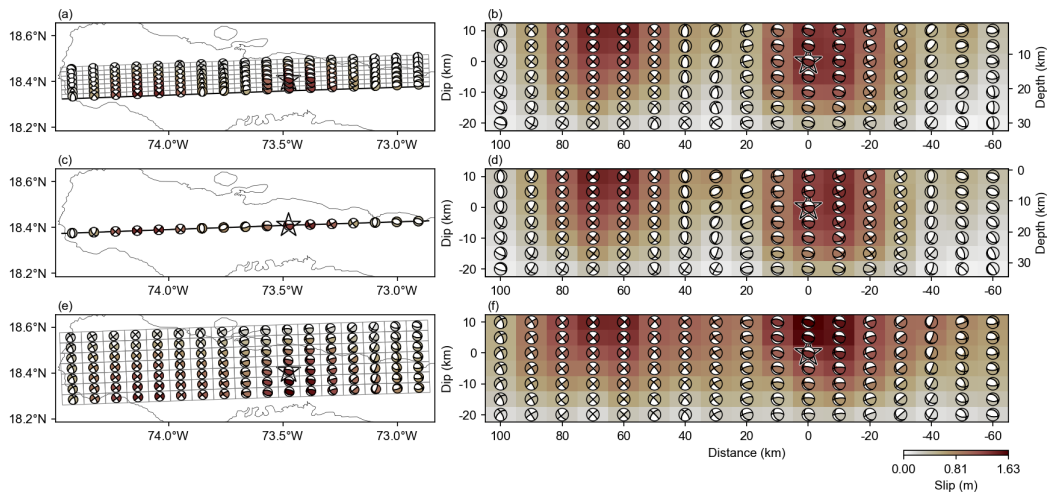


Figure S3. Finite-fault models of three different model-domain geometries using dipping planes of (a,b) 64°, (c,d) 90°, and (e,f) 0°. The horizontal model domain (e,f) is placed at 10-km depth.

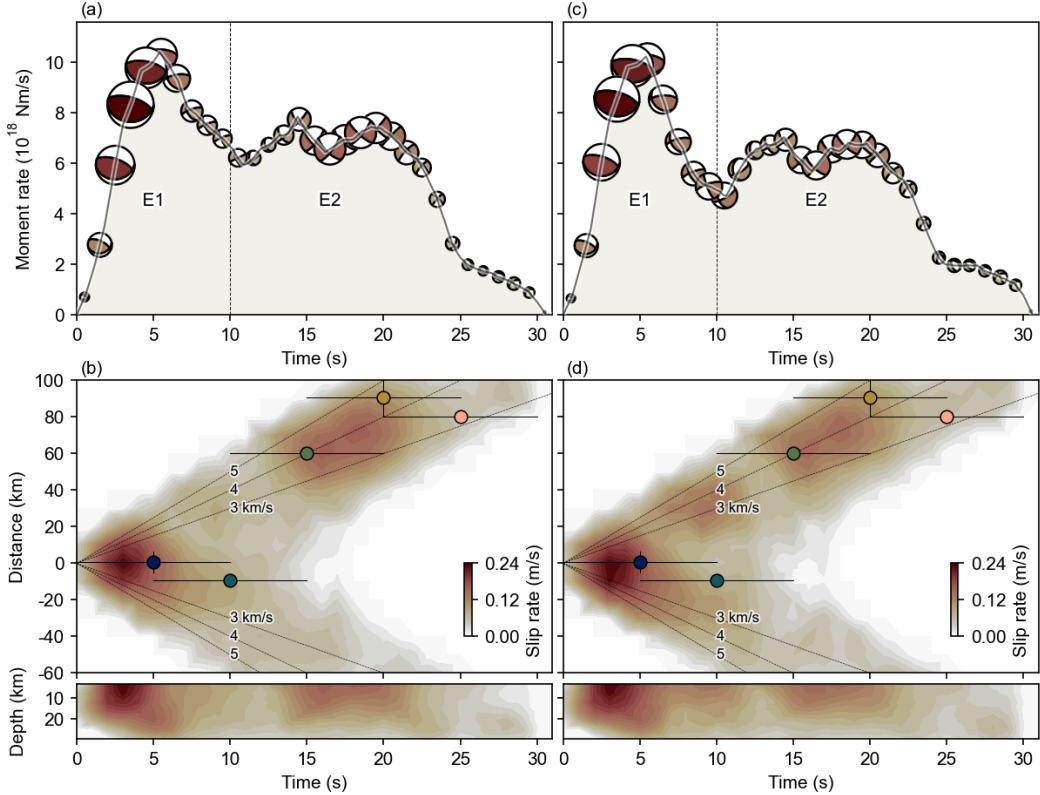


Figure S4. Resolvability test for the finite-fault inversion. (a,b) show the input model (Fig. 3) and (c,d) show the output model. (a,c) The moment rate functions of the finite-fault models. The beach balls are the centroid moment tensor solutions of the finite-fault models for the snapshot time windows of every 1 s. (b,d) The spatiotemporal distributions of the finite-fault model in comparison with the back-projection results. The distributions are projected along a direction of 268° azimuth (middle panel) and along the depth of the finite-fault model domain (bottom panel). The contours show the slip rate distributions. The colored dots are from the back-projection results. The vertical bars show the uncertainty estimates from the jackknife re-sampling exercise and the horizontal bars show the stacking window lengths. The black lines are the reference rupture speeds.

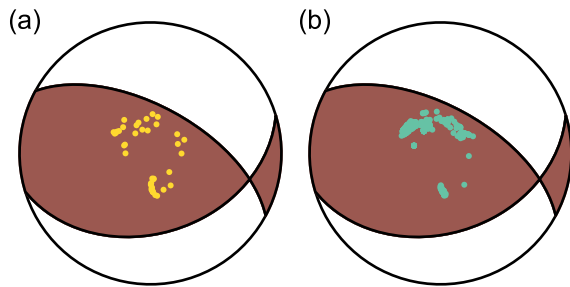


Figure S5. Station distributions used for (a) finite-fault and (b) back-projection analyses. The station locations are projected as yellow (finite-fault model) and green (back-projection) dots at the P wave ray piercing points at the lower focal sphere. The beach ball is the double-couple solution of the centroid moment tensor shown in Fig. 2b at 0–1 s.

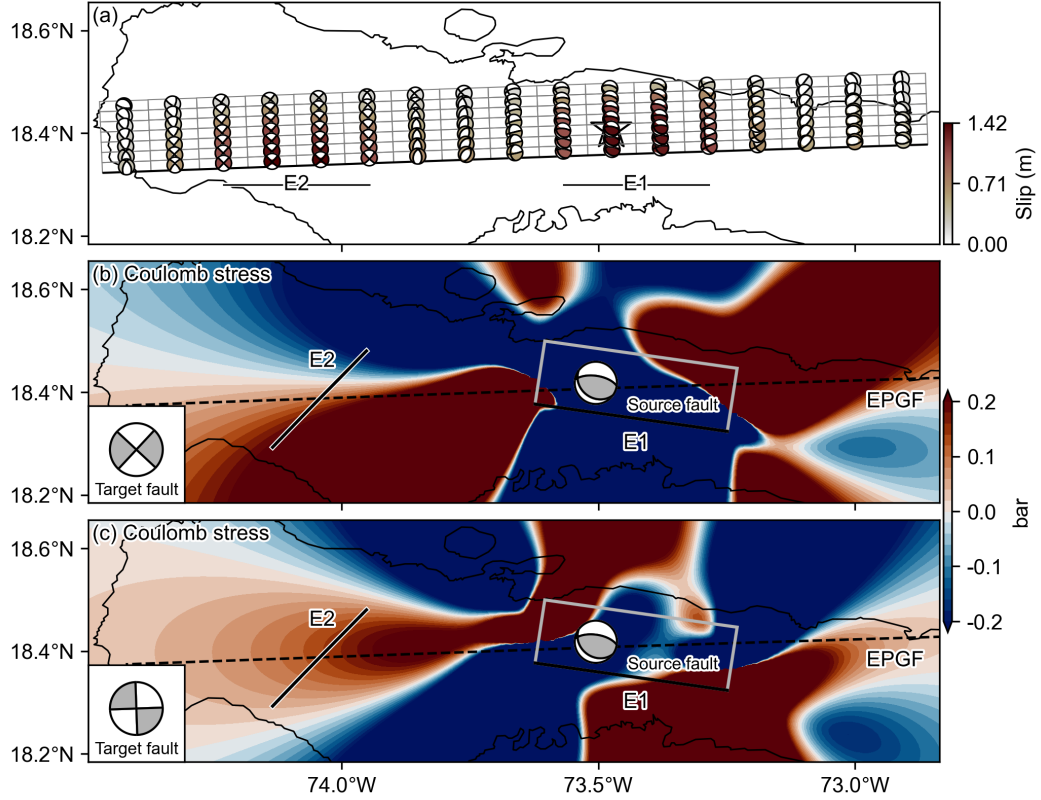


Figure S6. Coulomb stress analyses of the 2021 Haiti earthquake. (a) The optimal finite-fault solution of the 2021 Haiti earthquake as shown in Fig. 1. Lower panels show the Coulomb stress changes at 10-km depth for a target fault geometry of (b) $223^\circ/90^\circ/0^\circ$ (strike/dip/rake) and the EPGF geometry of (c) $268^\circ/90^\circ/0^\circ$. The Coulomb stresses are calculated with a friction coefficient of 0.4, poison ratio of 0.25, and Young's modulus of 8×10^5 bars. The source fault geometry is set as $278.4^\circ/62.7^\circ/77.1^\circ$ with an extent of 40-km in length and 30-km in width. The shallow edge of the source fault is at 0.8-km depth. We assume a uniform slip of 1.37 m for the source fault based on our rupture episode E1 (Fig. 1). The E2 location is outlined by a solid black line.

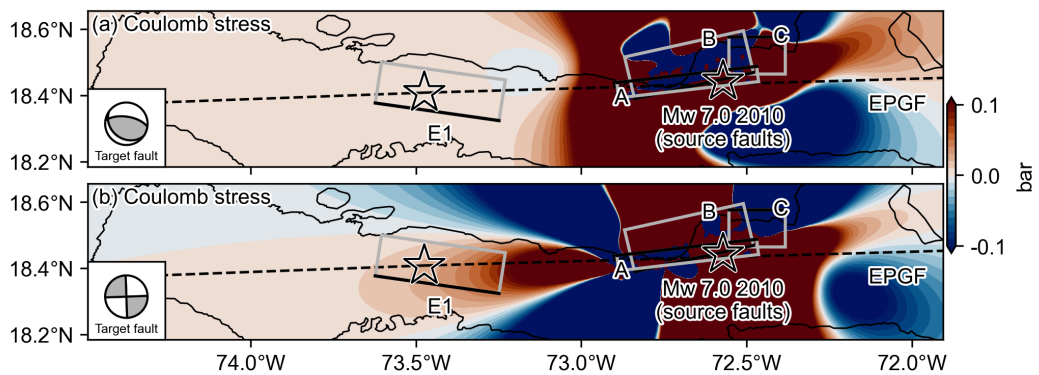


Figure S7. Coulomb stress analyses of the 2010 Haiti earthquake. Coulomb stress changes at 12-km depth on a target fault (a) of $278.4^\circ/62.7^\circ/77.1^\circ$ (strike/dip/rake) as E1 and the EPGF geometry (b) of $268^\circ/90^\circ/0^\circ$. The Coulomb stresses are calculated with a friction coefficient of 0.4, poison ratio of 0.25, and Young's modulus of 8×10^5 bars. The source fault geometries of the 2010 Haiti earthquake are from Hayes et al. (2010). The finite-fault model of the 2010 Haiti earthquake is from Hayes et al. (2010) archived at SRCMOD (Mai & Thingbaijam, 2014) (<http://quake-rc.info/SRCMOD/searchmodels/viewmodel/s2010HAITIx01HAYE/>). For the 2010 Haiti earthquake, we assume a pure vertical slip for fault B and left-lateral slip for faults A and C based on the model of Hayes et al. (2010).

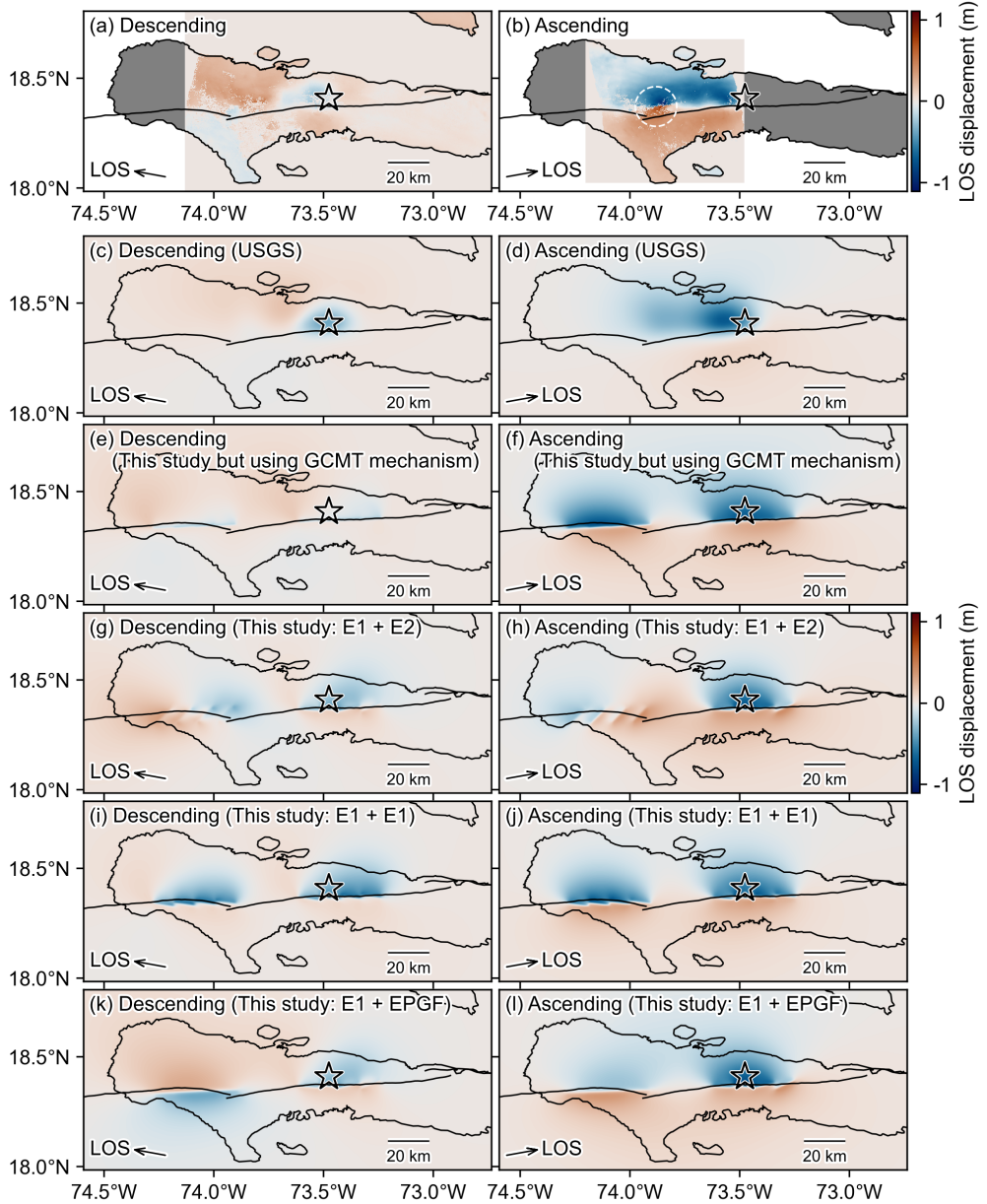


Figure S8. Line-of-sight (LOS) displacement maps from ALOS-2/PALSAR-2 (a) descending and (b) ascending tracks processed by Geospatial Information Authority of Japan (2021). Interferometric differences are between December 10, 2019 and August 17, 2021 for the descending frame, and between December 23, 2020 and August 18, 2021 for the ascending frame. The dashed circle in Fig. S8b highlights the largest deformation area and the oblique lineament cutting through an EPGF strand. The LOS displacement maps predicted by (c,d) the USGS NEIC finite-fault solution (U.S. Geological Survey Earthquake Hazards Program, 2017), (e,f) a model fixing the subfaults as having the GCMT focal mechanism (Dziewonski et al., 1981; Ekström et al., 2012) but with our obtained moments, (g,h) our preferred finite-fault solution, (i,j) a model fixing the E2 strike as that of the E1 and keeping the remaining parameters the same as our preferred finite-fault solution, and (k,l) a model fixing the E2 strike as that of EPGF (268°) and keeping the remaining parameters the same as our preferred finite-fault solution. The arrows show the LOS direction. The star shows the epicenter of the 2021 Haiti earthquake. The black lines show active faults in the region (Styron et al., 2020).

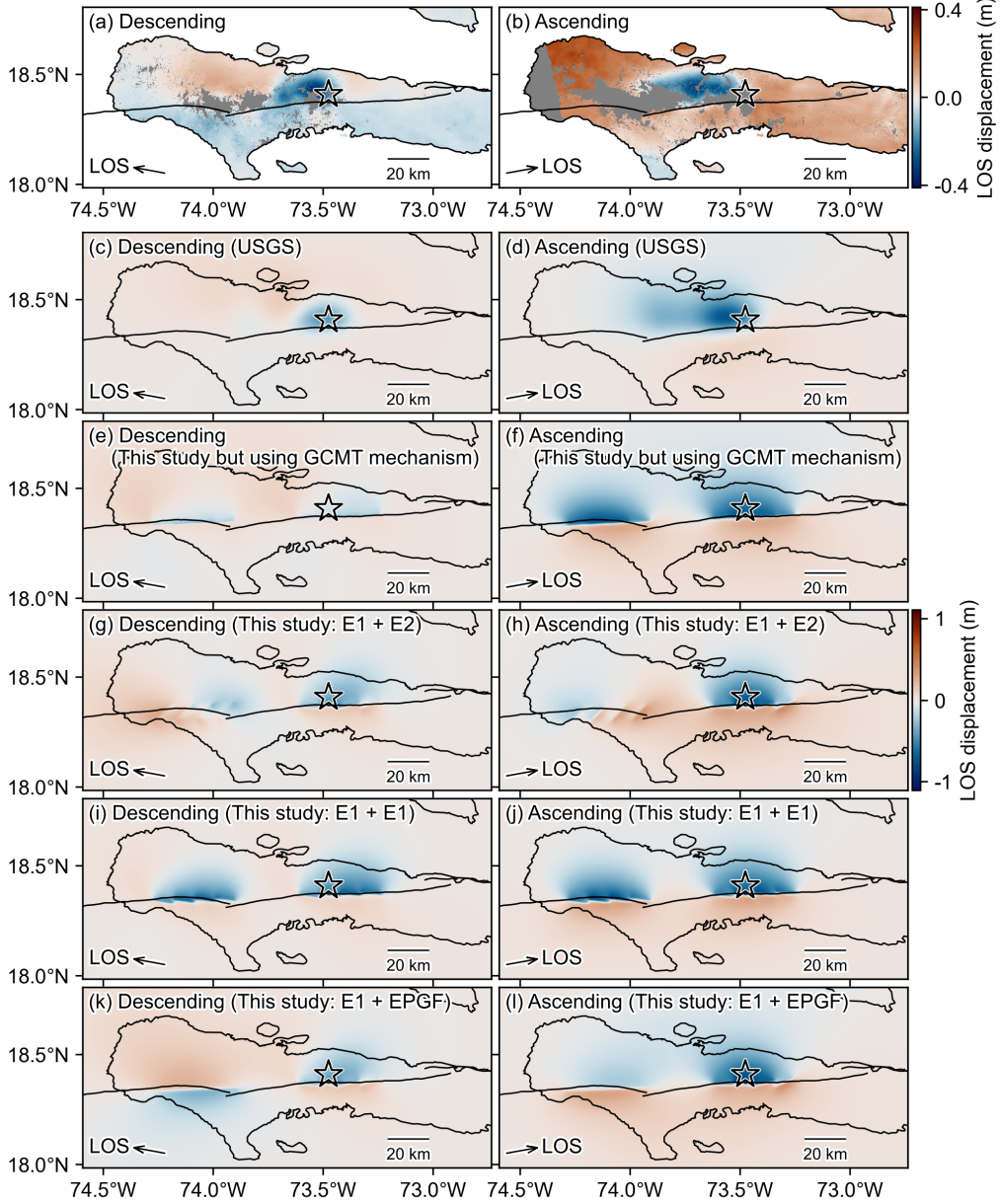


Figure S9. Line-of-sight (LOS) displacement maps from Sentinel-1 (a) descending and (b) ascending tracks processed by NASA/JPL-Caltech/Copernicus (2021). Interferometric differences are between August 3, 2021 and August 15, 2021 for the descending frame, and between August 5, 2021 and August 17, 2021 for the ascending frame. The LOS displacements maps predicted by (c,d) the USGS NEIC finite-fault solution (U.S. Geological Survey Earthquake Hazards Program, 2017), (e,f) a model fixing the subfaults as having the GCMT focal mechanism (Dziewonski et al., 1981; Ekström et al., 2012) but with our obtained moments, (g,h) our preferred finite-fault solution, (i,j) a model fixing the E2 strike as that of the E1 and keeping the remaining parameters the same as our preferred finite-fault solution, and (k,l) a model fixing the E2 strike as that of EPGF (268°) and keeping the remaining parameters the same as our preferred finite-fault solution. The arrows show the LOS direction. The star shows the epicenter of the 2021 Haiti earthquake. The black lines show active faults in the region (Styron et al., 2020).

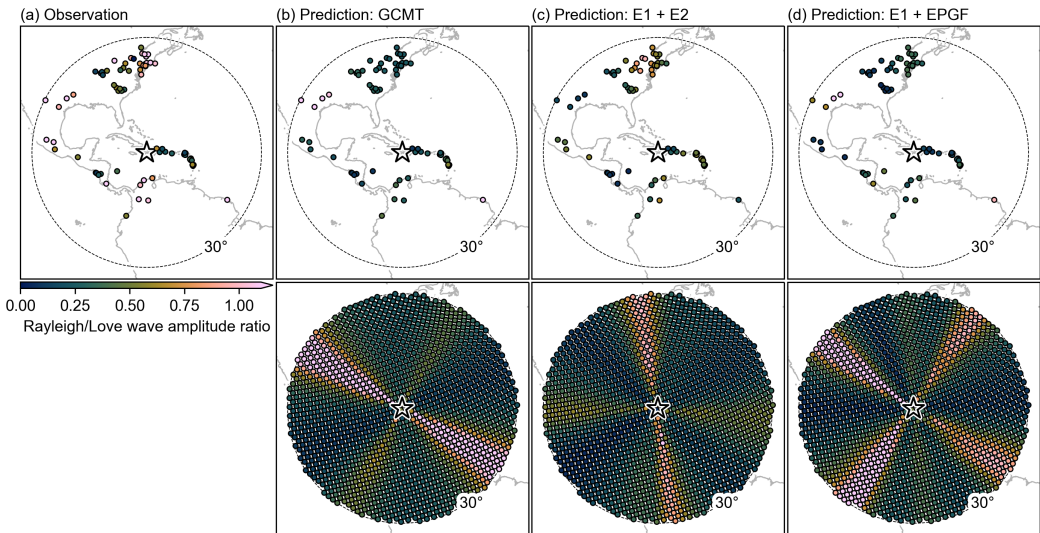


Figure S10. Comparison of Rayleigh-to-Love wave amplitude ratios for stations within 30° epicentral distance. (a) observation, (b) prediction from the GCMT solution (Dziewonski et al., 1981; Ekström et al., 2012), (c) prediction from our finite-fault solution (Fig. 1b), and (d) similar to Fig. S10c, but using the EPGF strike (268°) for the E2 domain. The bottom panels are similar to the top panels but for evenly spaced virtual stations. We compute synthetic waveforms using Instaseis method (van Driel et al., 2015). The Instaseis method uses a pre-computed Green's function database, which is calculated by the axisymmetric spectral-element code AxiSEM with the anisotropic version of the PREM model up to 5 s (Dziewonski & Anderson, 1981; Nissen-Meyer et al., 2014) and can be directly obtained from IRIS DMC Syngine (Krischer et al., 2017). The star shows the epicenter of the 2021 Haiti earthquake. The dashed line is an epicentral distance at 30° .

References in the Supporting Information

- Dziewonski, A. M., & Anderson, D. L. (1981). Preliminary reference Earth model. *Phys. Earth Planet. Inter.*, 25(4), 297–356. Retrieved from <http://www.sciencedirect.com/science/article/pii/0031920181900467> <https://linkinghub.elsevier.com/retrieve/pii/0031920181900467> doi:10.1016/0031-9201(81)90046-7
- Dziewonski, A. M., Chou, T.-A., & Woodhouse, J. H. (1981). Determination of earthquake source parameters from waveform data for studies of global and regional seismicity. *J. Geophys. Res. Solid Earth*, 86(B4), 2825–2852. doi:10.1029/JB086iB04p02825
- Ekström, G., Nettles, M., & Dziewoński, A. (2012). The global CMT project 2004–2010: Centroid-moment tensors for 13,017 earthquakes. *Phys. Earth Planet. Inter.*, 200–201, 1–9. doi:10.1016/j.pepi.2012.04.002
- Geospatial Information Authority of Japan. (2021). *The 2021 Haiti Earthquake: Crustal deformation detected by ALOS-2 data.* (<https://www.gsi.go.jp/cais/topic20210814-e.html>)
- Hayes, G. P., Briggs, R. W., Sladen, A., Fielding, E. J., Prentice, C., Hudnut, K., ... Simons, M. (2010). Complex rupture during the 12 January 2010 Haiti earthquake. *Nat. Geosci.*, 3(11), 800–805. doi:10.1038/ngeo977
- King, G. C., Stein, R. S., & Lin, J. (1994). Static stress changes and the triggering of earthquakes. *Bull. Seismol. Soc. Am.*, 84(3), 935–953. doi:10.1785/BSSA0840030935
- Krischer, L., Hutko, A. R., van Driel, M., Stähler, S., Bahavar, M., Trabant, C., & Nissen-Meyer, T. (2017). On-Demand Custom Broadband Synthetic Seismograms. *Seismol. Res. Lett.*, 88(4), 1127–1140. Retrieved from <https://doi.org/10.1785/0220160210> <https://pubs.geoscienceworld.org/srl/article/88/4/1127-1140/354100> doi:10.1785/0220160210
- Lin, J., & Stein, R. S. (2004). Stress triggering in thrust and subduction earthquakes and stress interaction between the southern San Andreas and nearby thrust and strike-slip faults. *J. Geophys. Res. Solid Earth*, 109(B2), 1–19. doi:10.1029/2003jb002607
- Mai, P. M., & Thingbaijam, K. K. (2014). SRCMOD: An online database of finite-fault rupture models. *Seismol. Res. Lett.*, 85(6), 1348–1357. doi:10.1785/0220140077
- NASA/JPL-Caltech/Copernicus. (2021). *Satellite Data Shows Ground Motion from August 2021 Haiti Earthquake.* Retrieved from <https://www.jpl.nasa.gov/images/pia23697-satellite-data-shows-ground-motion-from-august-2021-haiti-earthquake> (<https://www.jpl.nasa.gov/images/pia23697-satellite-data-shows-ground-motion-from-august-2021-haiti-earthquake>, https://aria-share.jpl.nasa.gov/20210814-Haiti_EQ/Displacements/)
- Nissen-Meyer, T., van Driel, M., Stähler, S. C., Hosseini, K., Hempel, S., Auer, L., ... Fournier, A. (2014). AxiSEM: broadband 3-D seismic wavefields in axisymmetric media. *Solid Earth*, 5(1), 425–445. Retrieved from <https://se.copernicus.org/articles/5/425/2014/> doi:10.5194/se-5-425-2014
- Styron, R., García-Pelaez, J., & Pagani, M. (2020). CCAF-DB: The Caribbean and Central American active fault database. *Nat. Hazards Earth Syst. Sci.*, 20(3),

- 831–857. doi:10.5194/nhess-20-831-2020
- Toda, S., Stein, R. S., Richards-Dinger, K., & Bozkurt, S. B. (2005). Forecasting the evolution of seismicity in southern California: Animations built on earthquake stress transfer. *J. Geophys. Res. Solid Earth*, 110(5), 1–17. doi:10.1029/2004JB003415
- U.S. Geological Survey Earthquake Hazards Program. (2017). *Advanced National Seismic System (ANSS) Comprehensive Catalog of Earthquake Events and Products*. doi:10.5066/F7MS3QZH
- van Driel, M., Krischer, L., Stähler, S. C., Hosseini, K., & Nissen-Meyer, T. (2015). In staseis: instant global seismograms based on a broadband waveform database. *Solid Earth*, 6(2), 701–717. Retrieved from <https://se.copernicus.org/articles/6/701/2015/> doi:10.5194/se-6-701-2015
- Wang, J., Xu, C., Freymueller, J. T., Wen, Y., & Xiao, Z. (2021). AutoCoulomb: An automated configurable program to calculate coulomb stress changes on receiver faults with any orientation and its application to the 2020 Mw7.8 Simeonof Island, Alaska, Earthquake. *Seismol. Res. Lett.*, 92(4), 2591–2609. doi:10.1785/0220200283